

Microstructural analysis of flash-healed Vickers-indented microcracks near positive/negative electrodes on the (001) surface of cubic zirconia single crystals under direct current electric fields

Shunsuke KAYUKAWA^a, Yutaro KATSUYAMA^a, Ayu KODAIRA^a, Tomoharu TOKUNAGA^a, Koji MORITA^b, and Takahisa YAMAMOTO^{a,*}

^aDepartment of Materials Design Innovation Engineering, Nagoya University, Furo-cho, Chikusa-ku, Nagoya, 464-8603, Japan

^bResearch Center for Electronic and Optical Materials, National Institute for Materials Science, Sengen 1-2-1, Tsukuba, Ibaraki 305-0047, Japan

Corresponding author: T. Yamamoto; E-mail: yamamoto.takahisa.r2@f.mail.nagoya-u.ac.jp

Keywords: flash healing, microcrack, zirconia, microstructure, flash sintering

Abstract

Flash healing is a technique that uses power spikes to rapidly repair microcracks on ceramic surfaces. In this study, the microstructures of flash-healed Vickers-indented microcracks near the positive/negative electrodes under a DC electric field were examined by scanning transmission electron microscopy. The microstructural morphology near the positive electrode was almost identical to that of the microcracks located between both electrodes, as previously reported. However, a decrease in the degree of healing was observed near the negative electrode. This was attributed to the insufficient recovery of dislocations generated at the indentation state, which should have occurred in the initial stage of healing. The delay in dislocation recovery prevented contact between the inner surfaces of the microcracks and is possibly related to the increase in oxygen vacancies near the negative electrode.

1. Introduction

When oxide ceramics are heated using an electric field above a certain threshold, an electric power spike is generated at a temperature determined by the applied electric field [1]. This power spike is called a flash event and can be used to induce mass diffusion in a short period. For instance, flash sintering enabled the instantaneous densification of ceramic compacts by leveraging flash events [2-4].

Flash healing refers to an application of the accelerated mass diffusion caused by the flash event [5]. This technique is used to rapidly heal microcracks formed on ceramic surfaces. Morita et al. generated microcracks of approximately 20 μm in length on the surface of fully stabilized zirconia (FSZ) polycrystals by Vickers indentation and then employed flash healing [6, 7]. The microcracks were fully healed during the flash event, which lasted approximately 10 min. Furthermore, the degree of microcrack healing was 3 to 4 times greater after the flash event compared with thermal healing at the same sample temperature. These results suggest that both thermal and non-thermal effects contribute to the enhancement of mass diffusion during the flash event.

Kayukawa et al. investigated the microstructure of flash-healed Vickers-indented microcracks on the (001) surface of FSZ single crystals by scanning transmission electron microscopy (STEM) [8]. Although the surface of the microcrack was healed, many pores corresponding to the unhealed state remained in the crystal interior, along the initial microcrack portion. The degree of healing observed in FSZ single crystals is less than that in FSZ polycrystals. Furthermore, the crystallographic orientations on the two sides of the initial microcrack were completely recovered, exhibiting the original single-crystal orientation after flash healing, which means the residual pores are included inside the single crystal. They attributed the low degree of healing in FSZ single crystals to the complete restoration of the crystallographic orientation because the residual pores must undergo slow lattice diffusion to annihilate. They

1 claimed that the presence of grain boundaries plays an important role as diffusion pathways in
2 the degree of healing. This was confirmed by Morita et al., who showed that the degree of
3 healing decreases as the grain size of FSZ polycrystals increases [7].
4
5

6
7 Thus, microstructural analysis provides valuable insight and helps clarify the mechanism of
8 flash healing. However, microstructural analysis of flash-healed microcracks in FSZ single
9 crystals has only been conducted on microcracks formed at the center of the sample between
10 both electrodes, even when a direct current (DC) electric field is used for flash healing. There
11 is a positional dependence along the direction of a DC electric field, including the sample
12 temperature [9], grain size [10-12], and microstructure [13-15]. For instance, the sample
13 temperature is generally lower near the negative electrode than at the central position [9], and
14 grain growth is accelerated by the formation of oxygen vacancies near the negative electrode
15 side [11]. Notably, oxygen vacancies are induced by the negative potential during flash healing
16 [16-18]. Therefore, we analyzed the microstructures of microcracks near the positive and
17 negative electrodes used during flash healing under a DC electric field and observed the
18 dependence of the microstructures on position.
19
20
21
22
23
24
25
26
27
28
29
30
31
32
33
34
35
36
37
38
39
40
41
42
43
44
45
46
47
48
49
50
51
52
53
54
55
56
57
58
59
60
61
62
63
64
65

2. Materials and Methods

Commercially available yttria FSZ single crystals (10 mol% $\text{Y}_2\text{O}_3\text{--ZrO}_2$, Shinkosha Co., Ltd., Japan) were used herein. The samples used for flash healing were machined from the purchased single crystal to have the dimensions of $0.5\text{ mm} \times 2\text{ mm} \times 10\text{ mm}$, in which a (001) surface of $2\text{ mm} \times 10\text{ mm}$ was mirror-finished by the manufacturer. The microcracks were formed perpendicular to the (001) surface by Vickers indentation using a micro-Vickers indenter (Via-S, Matsuzawa Co., Ltd.) at a load of 100 gf applied for 15 s. The indents were formed at a distance of approximately 2 mm from the positive and negative electrodes, as schematically shown in Fig. 1(a). As previously reported, microcracks generated by Vickers indentation are formed along the [110] and $[1\bar{1}0]$ directions, nearly vertical to the (001) single-crystal surface. Figure 1(c) shows a representative optical micrograph taken from the indent with a microcrack near a negative electrode. The average length of the diagonal dimensions of the indent was approximately $11.7\text{ }\mu\text{m}$, and the average half-length of the microcrack measured from the center of the indent was approximately $22.5\text{ }\mu\text{m}$.

After indentation, the samples were set in a high-temperature dilatometer (EVO2 TMA8311, Rigaku, Japan) modified to apply an electric field [19]. Platinum (Pt) sheets were used as the electrodes on both longitudinal faces of the samples, and no Pt paste was used. After setting, the samples were flash healed under DC electric fields (Asterion AST-751, AMETEK.com) using a conventional flash experimental protocol, namely the voltage-to-current protocol [20]. A DC electric field of 100 V/cm was applied under a limiting current of 150 mA/cm^2 , which is similar to the condition used in our previous study [8]. After the flash event occurred, the furnace temperature was kept constant for 10 min under the constant electric field. The power supply and furnace were then switched off and the samples were furnace-cooled to room temperature. The time for cooling to room temperature was approximately 20 min.

The surface morphology and topology in the vicinity of the indents near both electrodes were observed by scanning electron microscopy (SEM, MI4000L, Hitachi High-Tech Corp.) under a low acceleration voltage of 1 kV to increase the surface sensitivity, in addition to confocal optical microscopy (OPTELICS HYBRID +, Lasertec Corp.). Furthermore, the microstructure along healed microcracks inside the single crystal was observed by STEM (ARM-200FC, JEOL Ltd.) at an acceleration voltage of 200 kV. For STEM observation, thin STEM foils were prepared using a focused ion beam (FIB, Ethos NX5000, Hitachi High-Tech Corp.) to enable observation in the direction parallel to the original microcrack plane, and the details are shown in Fig. 1(b). The thickness of the thin STEM foils was adjusted to approximately 60 nm during the FIB process, which is similar to the thickness used in our previous reports [8, 21].

3. Results

3.1. Surface microstructure of flash-healed microcracks

A typical power spike was confirmed to occur under the present experimental condition, as previously described [8], in which the flash temperature was approximately 740 °C. From an equation based on a black-body radiation model [22], the sample temperature during the steady state after a flash event was roughly calculated to be 1250 °C. The detailed trend of electric power dissipation is described in Fig. S1 of the supplementary information.

Figure 2 shows (a) – (c) SEM images of the Vickers-indented areas, (d) – (f) magnified SEM images that include the edges of the Vickers indents, and the (g) – (i) height profiles obtained along the white lines indicated in the SEM images of (a) – (c), respectively, in which the height profiles were measured by confocal microscopy. The dotted lines in the height profiles show the depth at the tip of the pristine Vickers indent before flash healing, as described in Fig. S2 of the supplementary information, in which the value of variation in depth per indentation was within approximately 2.5% of the averaged value. The panels of (a), (d), and (g) are taken from Vickers indents formed near the positive electrode, and those of (c), (f), and (i) are taken from Vickers indents formed near the negative electrode. The data presented in (b), (e), and (h) are similar to those reported in our previous study [8], which were taken from Vickers indents formed in the central area between both electrodes, as presented in Fig. 1(a).

Flat and sharp microcracks are generated from the respective four corners of the indent, in which a square-shaped indent is formed with sides along the $[100]$ and $[0\bar{1}0]$ directions and the microcracks are generated along the $[110]$ and $[1\bar{1}0]$ directions, as presented in Fig. S2 of the supplementary information. In contrast, SEM images show that the surfaces of the microcracks are healed after flash healing. However, the degree of healing at the surfaces is different, as presented in (d) – (f), in which a flattened surface is observed near the positive side in (d), a

1 slightly concaved surface is observed at the center in (e), and a thready lined surface is observed
2 at the negative side in (f). In addition, after flash healing, material up-lift is generated around
3 the indents, as presented by a white block arrow in (b). The depth of the indent tip from the
4 surface outside the material up-lift area becomes shallower with the indent position from the
5 negative side to the positive side, in which all the depths are shallower than those of a pristine
6 sample, as indicated by the dotted lines in the panels of (g) – (i) (also shown in Fig. S2 of the
7 supplementary information). This variation in morphology suggests that the degree of healing
8 depends on the position along the DC electric field direction, from the positive to the negative
9 electrode.

10 3.2. *Microstructure of flash-healed microcracks inside crystals*

11 Cross-sectional high-angle annular dark-field (HAADF)-STEM observations of the healed
12 microcrack on the positive side are shown in Fig. 3. A row of pores can be seen along the
13 original microcrack, as indicated by the black arrow in the image, revealing that the microcrack
14 has not been completely healed inside the crystal. However, the high-density dislocations that
15 occur during Vickers indentation are not observed around the row of pores after flash healing.
16 As presented in a magnified HAADF-STEM image in Fig. 3(c), the pores have a rectangular
17 shape. The shape is composed of $(\bar{1}11)$ and $(\bar{1}\bar{1}\bar{1})$ side planes and (110) upper/lower basal planes,
18 which are planes with small surface energy in cubic zirconia [23,24]. As indicated in the
19 selected area diffraction (SAD) pattern for the crystal areas on both sides of the healed
20 microcrack, the crystallographic orientation was completely recovered, displaying the original
21 relationship for the single crystal. These results are similar to those obtained for the indent
22 formed in the central region of the single crystal [8].

23 On the negative side, not only the degree of healing but also the microstructure around the
24 original microcrack was significantly different from those on the positive side. The

microstructural analysis results for flash-healed microcracks on the negative side are presented in Figs. 4–6. The crystallographic features are shown in the SAD pattern (Fig. 4(b)), and diffraction spot separation is observed, for example, at the $\bar{2}24$ diffraction spot (Fig. 4(c)). This slight misfit angle was less than approximately 0.3° with respect to the $[110]$ axis. The original single-crystal orientation on both sides of the microcrack was not completely recovered near the negative electrode, unlike the microcracks near the positive electrode (Fig. 3(b)). Furthermore, as shown in Fig. 4(d), a slight increase in the angle between the 002 and $\bar{2}20$ diffraction spots, which should be 90° in a fluorite structure of FSZ, was observed [25]. These crystallographic features are attributed to the oxygen vacancies formed on the negative side and the incomplete recovery of dislocations formed during indentation as explained later.

In addition to these crystallographic features, microstructural features are also observed, including different pore morphology (arrows B and C), the appearance of numerous linear contrasts around the healed microcrack (arrow D), and the existence of a linear gap (arrow A).

As for the shapes of pores, magnified images are shown in Fig. 5, in which (a) and (b) are taken from the area indicated by arrow B in Fig. 4(a), and (c) and (d) are taken from the area indicated by arrow C in Fig. 4(a). The pore shapes in the near-surface region, indicated by arrow B, are either rounded rhomboids or other rounded forms. These shapes are different from the rhombic shapes observed on the positive side (Fig. 3(c)). The pores on the positive side have habit planes that make up the shape and are distinctively visible. The difference in the pore shape is probably related to a change in surface energy. As shown in the high-resolution (HR)-HAADF-STEM image (Fig. 5(b) and (d)), there is no formation of a second phase in any of the pores.

As for the numerous linear contrasts, high magnification HAADF-STEM observation reveals that the structure with linear contrast is composed of an array of numerous pores. Figure 6

shows magnified HAADF-STEM images taken from the structure with curved line contrast, as presented by arrow D in Fig. 4(a). The structure with linear contrast in the low magnification image is confirmed to be composed of numerous rectangular pores, as shown in Fig. 6(a). As observed in the HR-HAADF-STEM image (Fig. 6(b)), these rectangular pores form thin plates (i.e., laminates), and no secondary phase with a different structure is formed. The sides of the rectangular pores are $(\bar{1}11)$ and $(\bar{1}\bar{1}\bar{1})$ planes, which are similar to those of the pores that remained along the unhealed microcracks observed on the positive side. In addition, the compositional analysis of the areas including the rectangular pores (white boxes in Figs. 5(d) and 6(b)) revealed that nitrogen was present (Fig. 6(c)). However, the crystals exhibit the fluorite structure of FSZ, indicating that the detected nitrogen forms solutes in the FSZ structure. It has been reported that zirconia is nitrided during flash sintering under a DC electric field [19, 26, 27]. Morisaki et al. reported that the nitridation of zirconia is possibly a result of the strongly reduced state caused by a DC electric field [19]. The solid solution of nitrogen shown in Fig. 6(c) was observed on the negative side, suggesting that a strong reduction state occurred on the negative side, similar to previous reports [19].

Finally, the gap indicated by arrow A in Fig. 4(a) is related to the incomplete recovery of the crystallographic orientation on both sides of the microcrack. As for this issue, it will be discussed later.

4. DISCUSSION

4.1 Healing near the positive electrode

The microstructure of microcracks on the positive side after flash healing is similar to that typically observed at the center of the single crystals [8]. As shown in Fig. 3, the microcrack was not completely healed, and numerous pores were present along the original microcrack. These pores are flat and have a near-rhombic shape comprised of $(\bar{1}11)$ and $(\bar{1}\bar{1}\bar{1})$ side planes and (110) basal planes. These planes are consistent with the low surface energy planes reported for FSZ [23,24]. After healing, the crystals on both sides of the microcracks were completely recovered to their original single-crystal orientation.

Figure 7 shows the healing ratio estimated from a sum of pore diameters along the healed microcrack, including previously reported data (see the schematic inset in Fig. 7 for the calculation method of the healing ratio) [8]. The results on the positive side are indicated by a red dot in the plot. The healing ratio was approximately 55%, which is similar to that obtained under the other conditions shown in Fig. 7. Considering that the crystallographic orientations on both sides of the microcracks are completely restored to that of the original single crystal, the pores formed in the early stages of healing must undergo lattice diffusion to subsequently annihilate. In the case of polycrystalline FSZ, grain boundary diffusion, which is faster than lattice diffusion, effectively serves as a diffusion pathway for pore annihilation. However, in single crystals, the pore must undergo lattice diffusion, and the annihilation rate inside the crystal, far from the surface, is extremely small. At this time, only the change in the distribution of pore diameter due to Ostwald ripening is noticeable, and the decrease in its total volume is slow. As shown in Fig. 7, the healing ratio does not change significantly, even on the positive electrode side where the sample temperature is considered to be higher [9].

4.2 Healing near the negative electrode

The microstructure on the negative side was significantly different from that of healed

microcracks reported previously [8,21]. As mentioned above, the solid solution of nitrogen on the negative side is indicative of a strongly reduced state there. The existence of oxygen vacancies corresponding to this strongly reduced state may be involved in the microstructure formation on the negative side. Although the microstructure on the negative side cannot be strictly discussed at this time, it is inferred as follows.

4.2.1 Numerous arrays of rectangular laminate pores

Figure 8(a) and (b) shows the SEM and bright-field transmission electron microscopy (TEM) images of the area just below the indent on the pristine sample, in which the thin TEM foil was cross-sectionally obtained by FIB. As shown in Fig. 8(a), many curved line contrasts are observed in the area just below the indent (white arrows). These line contrasts are similar to those shown in Fig. 4(a) (arrow D). The TEM bright-field image (Fig. 8(b)) taken from this area shows no microcracks in the field of view, and a densely formed dislocation structure is observed [28,29]. In this dislocation structure, linear contrasts can be seen near tangled dislocations (white arrows in Fig. 8(b)).

The microstructural morphology with an array of pores shown in Fig. 6 may appear similar to that with a row of pores after healing, as shown in Fig. 3. However, as shown in Fig. 8, there were no additional microcracks in the area below the indent in the pristine sample. In other words, the linear contrast shown in Fig. 6, in which many rectangular laminate pores are arranged, is not the microstructure formed by the healing of microcracks.

The formation of numerous arrays of rectangular laminate pores along curved lines may be due to the trapping of oxygen vacancies in a severe reduction atmosphere. Oxygen vacancies are trapped and accumulated at the dislocations, and the accumulated oxygen vacancies may have aggregated with each other under the flash state to form rectangular laminate pores, as shown in Fig. 6(b). Furthermore, because these pores exist inside the single crystal, it is difficult to annihilate the pores after accumulation. This condition is similar, for example, to the

1 remaining pores observed in the healed area shown in Fig. 3. This characteristic pore structure
2 on the negative side cannot be observed on the positive side (Fig. 3) or in the central area. These
3 results indicate that the high-density dislocations generated during Vickers indentation are
4 quickly recovered during healing, except on the negative side. In other words, delayed recovery
5 of dislocations by oxygen vacancies is characteristic of the healing process on the negative side.
6
7 This delay may prevent the complete recovery of the original crystallographic orientation,
8 resulting in the linear gap that remains along the original microcrack, as indicated by arrow A
9 in Fig. 4(a).
10
11
12
13
14
15
16
17

18 4.2.2 *Healing behavior on the negative side*

19 On the negative side, it has been reported that mass diffusion is enhanced due to the formation
20 of oxygen vacancies. For example, Qin et al. examined the grained structure obtained during
21 flash sintering and reported that the grain size increases in the vicinity of the negative electrode
22 [12]. Dong et al. presented theoretical calculations showing that the diffusion barrier of cations
23 in the vicinity of oxygen vacancies is decreased [30, 31]. Considering these reports, it is
24 reasonable to assume that the healing rate of microcracks increases on the negative side. This
25 can be inferred from the fact that the remaining pores in the healed area on the negative side
26 are very fine, as shown in Fig. 5(c). However, the depth at the tip of the Vickers indent after
27 flash healing is deepest on the negative side, as shown in Fig. 2, suggesting that the degree of
28 healing on the negative side was less than that in the center and on the positive side. In other
29 words, the healing rate is faster on the negative side, but the resulting degree of healing is less.
30
31 This phenomenon is related to the delayed dislocation recovery described above.
32
33
34
35
36
37
38
39
40
41
42
43
44
45
46
47
48
49
50

51 For a microcrack formed on a single-crystal surface by indentation, the microcrack inside the
52 crystal remains open owing to the presence of numerous dislocations generated in the plastic
53 deformation region [28, 29]. To heal the microcracks, these dislocations must first be recovered,
54 before the microcracks can close. After that, their inner surfaces must come into contact to
55
56
57
58
59
60
61
62
63
64
65

1 initiate bonding by diffusion [32, 33]. As previously mentioned, during this initial healing
2 process, dislocation recovery only occurs partially on the negative side. The microcracks cannot
3 be completely closed because the generated strain prevents healing. The delay in dislocation
4 recovery is likely caused by the oxygen vacancies formed on the negative side, as shown in Fig.
5
6
7
8
9
10 6. Although a sample temperature difference occurs in the region near the positive/negative
11 electrodes when a DC electric field is used [9], the observed post-healed histological features
12 on the negative side are considered a characteristic phenomenon that occurs near the negative
13 electrode, rather than a phenomenon caused by the temperature difference.

14
15
16
17
18
19 Morita et al. investigated flash healing using polycrystalline FSZ and reported that the degree
20 of healing did not depend on indent positions with respect to the positive/negative electrodes
21 [7]. This may be attributed to the presence of grain boundaries that act as pathways for diffusion.
22
23
24 As a result, the high recovery rate did not cause a positional dependence. Moreover, the
25 dependence of the indent position may emerge when the grain size of the FSZ polycrystal
26 becomes sufficiently large.
27
28
29
30
31
32
33
34
35
36
37
38
39
40
41
42
43
44
45
46
47
48
49
50
51
52
53
54
55
56
57
58
59
60
61
62
63
64
65

5. Conclusions

Microcracks were generated using Vickers indentation on (001) surfaces of FSZ single crystals and then flash healed using a DC electric field. The microstructures near the positive and negative electrodes were analyzed by STEM. The results are outlined as follows.

(1) In the flash-healed microcracks near the positive electrode, the crystal orientations on both sides of the microcrack were completely recovered, exhibiting the original single-crystal orientation. Many residual pores corresponding to the unhealed state were observed along the original microcrack location. These pores had a rhombic shape with $\{111\}$ side and (110) basal planes, which correlate with a low surface energy in FSZ. This morphology was similar to those previously obtained in the microcracks at the center position between the electrodes of the samples after flash/thermal healing.

(2) The microstructure of the flash-healed microcracks near the negative electrode was significantly different from that obtained near the positive electrode and at the center position between the electrodes. Very small residual pores were dispersed in the crystal interior in the vicinity of the original microcrack location, and numerous dislocations were observed around the healed microcrack. In addition, a linear gap existed along the healed microcrack. The degree of healing was lower on the negative side than on the positive side. Furthermore, the crystallographic orientation on the two sides of the microcrack was not completely recovered. The decrease in the degree of healing was ascribed to the insufficient recovery of dislocations generated during the early stage of the healing process. The delayed recovery of the dislocations was likely related to the increased concentration of oxygen vacancies in the region near the negative electrode.

Acknowledgments

This work was financially supported by CREST (JPMJCR1996) from the Japan Science and Technology Agency, and JSPS KAKENHI (Grant Number JP19H05788). This work was supported in part by "Advanced Research Infrastructure for Materials and Nanotechnology in Japan (ARIM)" of the Ministry of Education, Culture, Sports, Science and Technology (MEXT).

References

1. M. Cologna, B. Rashkova, R. Raj, Flash sintering of nanograin zirconia in <5s at 850°C, J. Am. Ceram. Soc. 93 (2010) 3556–3559.
<https://doi.org/10.1111/j.1551-2916.2010.04089.x>.
2. O. Guillon, R.A. De Souza, T.P. Mishra, W. Rheinheimer, Electric- field- assisted processing of ceramics: nonthermal effects and related mechanisms, MRS Bull. 46 (2021) 52–58.
<https://doi.org/10.1557/s43577-020-00008-w>.
3. M. Yu, S. Grasso, R. Mckinnon, T. Saunders, M.J. Reece, Review of flash sintering: materials, mechanisms and modelling, Adv. Appl. Ceram. 116 (2017) 24–60.
<https://doi.org/10.1080/17436753.2016.1251051>.
4. M. Biesuz, V.M. Sglavo, Flash sintering of ceramics, J. Eur. Ceram. Soc. 39 (2019) 115–143.
<https://doi.org/10.1016/j.jeurceramsoc.2018.08.048>.
5. K. Morita, F. Naito, D. Terada, Microcrack healing in zirconia ceramics under a DC electric field/current, J. Eur. Ceram. Soc. 41 (2021) 282–289.
<https://doi.org/10.1016/j.jeurceramsoc.2021.09.044>.
6. S. Kawabata, S. Takahashi, K. Nambu, K. Morita, Effect of DC and AC electric fields on crack healing behavior in 8 mol% yttria- stabilized cubic zirconia polycrystal, J. Am. Ceram. Soc. 106 (2023) 6163–6176.
<https://doi.org/10.1111/jace.19269>.
7. S. Takahashi, K. Morita, K. Nambu, D. Terada, K. Kobayashi, T. Tokunaga, T. Yamamoto, Effect of Initial Grain Size on Crack Healing Behavior under DC Electric Field of Zirconia (8Y-CSZ) Ceramic, Adv. Eng. Mater. 25 (2023) 2201807.
<https://doi.org/10.1002/adem.202201807>.
8. S. Kayukawa, Y. Katsuyama, A. Kodaira, T. Tokunaga, K. Morita, A. Nakamura, T. Yamamoto, Flash healing of Vickers microcracks formed on the (001) surface of cubic zirconia single crystals, J. Eur. Ceram. Soc. 43 (2023) 6272–6278.
<https://doi.org/10.1016/j.jeurceramsoc.2023.06.001>.

- 1 9. G. Liu, D. Liu, J. Liu, Y. Gao, Y. Wang, Asymmetric temperature distribution during steady
2 stage of flash sintering dense zirconia, *J. Eur. Ceram. Soc.* 38 (2018) 2893–2896.
3 <https://doi.org/10.1016/j.jeurceramsoc.2018.02.012>.
4
5
6
- 7 10. T. P. Mishra, C. Lenser, R. Raj, O. Guillon¹, M. Bram, Development of a processing map
8 for safe flash sintering of gadolinium-doped ceria, *J. Am. Ceram. Soc.* 104 (2021) 4316–
9 4328.
10 <https://doi.org/10.1111/jace.17847>.
11
12
13
14
15
- 16 11. Y. Dong, H. Wang, I-W. Chen, Electrical and hydrogen reduction enhances kinetics in
17 doped zirconia and ceria: I. grain growth study, *J. Am. Ceram. Soc.* 100 (2017) 0876–886.
18 <https://doi.org/10.1111/jace.14615>.
19
20
21
22
23
- 24 12. W. Qin, H. Majidi, J. Yun, K. Benthem, Electrode Effects on Microstructure Formation
25 During FLASH Sintering of Yttrium-Stabilized Zirconia, *J. Am. Ceram. Soc.* 99 (2016)
26 2253–2259.
27 <https://doi.org/10.1111/jace.14234>.
28
29
30
31
- 32 13. W. Rheinheimer, X. L. Phuah, L. Porz, M. Scherer, J. Cho, H. Wang, The impact of flash
33 sintering on densification and plasticity of strontium titanate: high heating rates,
34 dislocation nucleation and plastic flow, *J. Euro. Ceram. Soc.* 43 (2023) 3524–3537.
35 <https://doi.org/10.1016/j.jeurceramsoc.2023.02.007>.
36
37
38
39
40
41
- 42 14. Y. Zhang, J.-I. Jung, J. Luo, Thermal runaway, flash sintering and asymmetrical
43 microstructural development of ZnO and ZnO–Bi₂O₃ under direct currents, *Acta Mater.*
44 94 (2015) 87–100.
45 <http://dx.doi.org/10.1016/j.actamat.2015.04.018>.
46
47
48
49
50
- 51 15. J.C. M'Peko, J. S.C. Francis, R. Raj, Field-assisted sintering of undoped BaTiO₃:
52 Microstructure evolution and dielectric permittivity, *J. Euro. Ceram. Soc.* 34 (2014) 3655–
53 3660.
54 <https://doi.org/10.1016/j.jeurceramsoc.2014.04.041>.
55
56
57
58
59
60

16. R.E.W. Casselton, Blackening in yttria stabilized zirconia due to cathodic processes at solid platinum electrodes, *J Appl Electrochem* 4 (1974) 25–48.
<https://doi.org/10.1007/BF00615903>.
17. D. A. Wright, J. S. Thorp, A. Aypar, H. P. Buckley, Optical absorption in current-blackened yttria-stabilized zirconia, *J. Mater. Sci.* 8 (1973) 876–882.
<https://doi.org/10.1007/BF02397918>.
18. M. Seko, S. Inagaki, T. Tokunaga, S. Kobayashi, A. Nakamura, T. Yamamoto, Applying an alternating current to strontium titanate minimizes the change in oxidation state caused by flash sintering, *J. Eur. Ceram. Soc.* 44 (2024) 2965–2971.
<https://doi.org/10.1016/j.jeurceramsoc.2023.12.046>.
19. N. Morisaki, H. Yoshida, K. Matsui, T. Tokunaga, K. Sasaki, T. Yamamoto, Synthesis of zirconium oxynitride in air under DC electric fields, *Appl. Phys. Lett.* 109 (2016) 083104.
<https://doi.org/10.1063/1.4961624>.
20. P. Kumar, M K. D. Yadav, J.-M. Lebrun, R. Raj, Flash sintering with current rate: A different approach, *J. Am. Ceram. Soc.* 102 (2019) 823–835.
<https://doi.org/10.1111/jace.16037>.
21. S. Kayukawa, Y. Katsuyama, A. Kodaira, T. Tokunaga, K. Morita, A. Nakamura, K. Higuchi, T. Yamamoto, Microcrack healing in single-crystal cubic zirconia by thermal annealing, *J. Eur. Ceram. Soc.* 43 (2023) 1078–1086.
<https://doi.org/10.1016/j.jeurceramsoc.2022.10.065>.
22. W. Ji, B. Parker, S. Falco, J. Y. Zhang, Z. Y. Fu, R. I. Todd, Ultra-fast firing: Effect of heating rate on sintering of 3YSZ, with and without an electric field, *J. Eur. Ceram. Soc.* 37 (2017) 2547–2551.
<https://doi.org/10.1016/j.jeurceramsoc.2017.01.033>.
23. A. Christensen, E.A. Carter, First-principles study of the surfaces of zirconia, *Phys.*

- Rev. B. 58 (1998) 8050–8058,
<https://doi.org/10.1103/PhysRevB.58.8050>.
24. G. Ballabio, M. Bernasconi, F. Pietrucci, S. Serra, Ab initio study of yttria-stabilized cubic zirconia surfaces, *Phys. Rev. B.* 70 (2004) 075417.
<https://doi.org/10.1103/PhysRevB.70.075417>.
25. I. R. Lavagnini, J. V. Campos, J. A. Ferreira, E. M. J. A. Pallone, Microstructural evolution of 3YSZ flash-sintered with current ramp control, *J. Am. Ceram. Soc.* 103 (2020) 3493–3499.
<https://doi.org/10.1111/jace.17037>.
26. T. Kurachi, Y. Yamashita, T. Tokunaga, T. Yamamoto, Flash Sintering of 3YSZ by Controlling a Wave Form of Electric Fields, *International Journal of Advanced Microscopy and Theoretical Calculations*, 6 (2019) 34–35.
27. C. Bechteler, R. I. Todd, Lattice modification of $\text{ZrO}_2\text{-}\delta$ and formation of rocksalt structure ZrO and Zr(O,N) after DC electrical loading of 3YSZ, *J. Eur. Ceram. Soc.* 44 (2024) 1044–1052.
<https://doi.org/10.1016/j.jeurceramsoc.2023.09.014>.
28. S. Huang, J.G.P. Binner, B. Vaidhyanathan, R.I. Todd, Quantitative analysis of the residual stress and dislocation density distributions around indentations in alumina and zirconia toughened alumina (ZTA) ceramics, *J. Eur. Ceram. Soc.* 34 (2014) 753–763.
<http://dx.doi.org/10.1016/j.jeurceramsoc.2013.09.021>.
29. D. Holmes, A.H. Heuer, P. Pirouz, Dislocation structures around Vickers indents in 9.4 mol% Y_2O_3 -stabilized cubic ZrO_2 single crystals, *Philos. Mag. A.* 67 (1993) 325–342.
<https://doi.org/10.1080/01418619308207161>.
30. Y. Dong, L. Qi, J. Li, I-W. Chen, A computational study of yttria-stabilized zirconia: II. Cation diffusion, *Acta Mater.* 126 (2017) 438–450.

<http://dx.doi.org/10.1016/j.actamat.2017.01.008>.

31. Y. Dong, L. Qi, J. Li, I-W. Chen, A computational study of yttria-stabilized zirconia: I. Using crystal chemistry to search for the ground state on a glassy energy landscape, *Acta Mater.* 127 (2017) 73–84.

<http://dx.doi.org/10.1016/j.actamat.2017.01.006>.

32. T.K. Gupta, Instability of Cylindrical Voids in Alumina, *J. Am. Ceram. Soc.* 61 (1978) 191-195.

<https://doi.org/10.1111/j.1151-2916.1978.tb09276.x>

33. T.K. Gupta, Crack Healing and Strengthening of Thermally Shocked Alumina, *J. Am. Ceram. Soc.* 59 (1976) 259-262.

<https://doi.org/10.1111/j.1151-2916.1976.tb10949.x>.

FIGURES

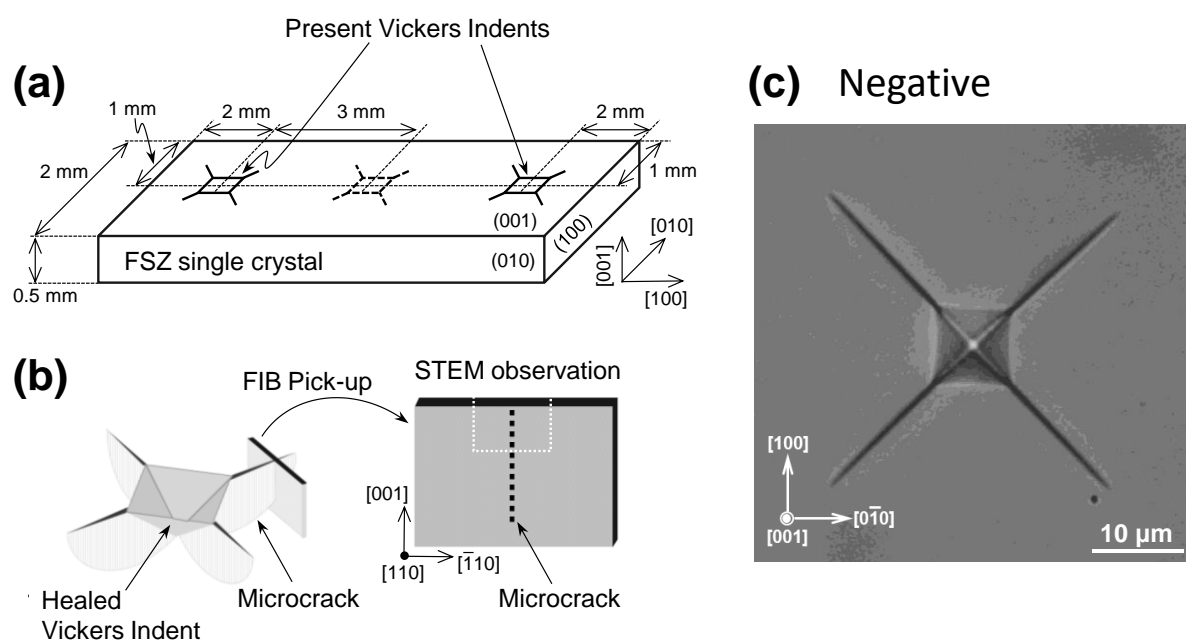


FIGURE 1

Schematic illustrations showing the (a) positions of Vickers indents on the (001) surface of FSZ single crystals with crystallographic orientation, (b) preparation of the thin STEM foil, and (c) an optical micrograph showing a pristine Vicker indent near the negative electrode.

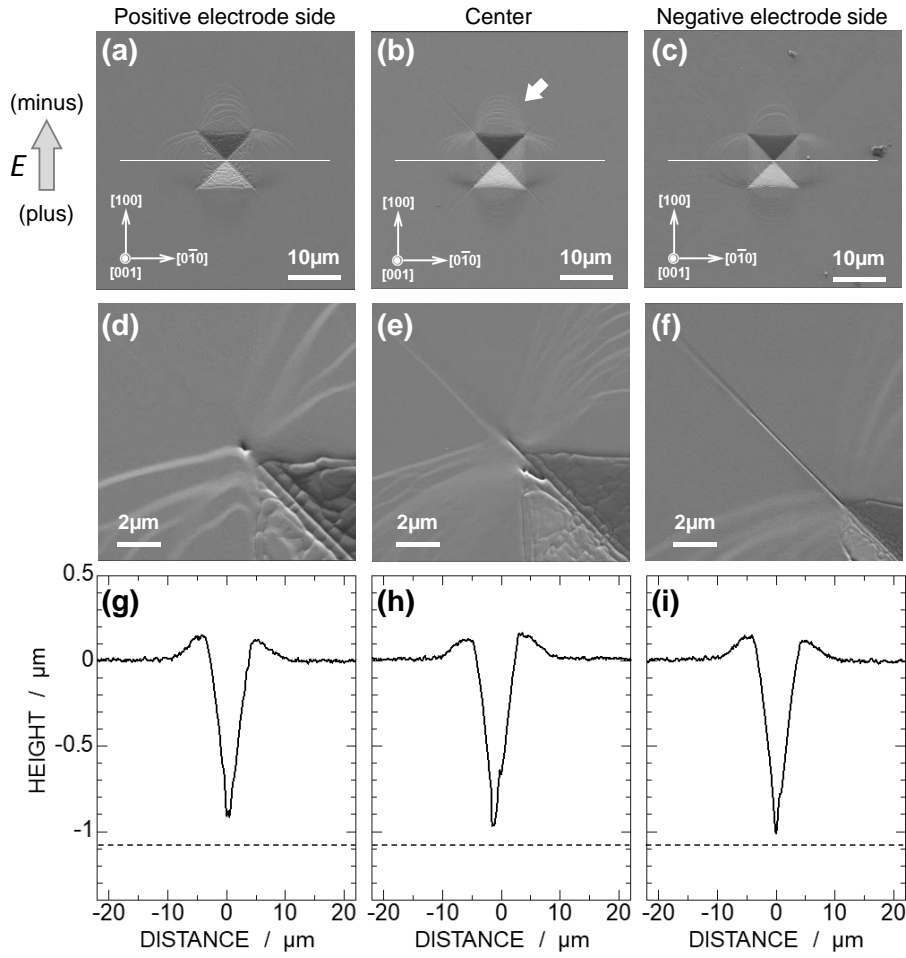


FIGURE 2

Surface structures and height profiles of flash-healed Vickers microcracks: (a), (d), (g) near the positive electrode, (b), (e), (h) at the center, and (c), (f), (i) near the negative electrode. SEM images of (a)-(c) show flash-healed Vickers indents, and (d)-(f) show magnified images around the edges of indents. Height profiles of (g)-(i) were measured along the white lines indicated in (a)-(c), respectively.

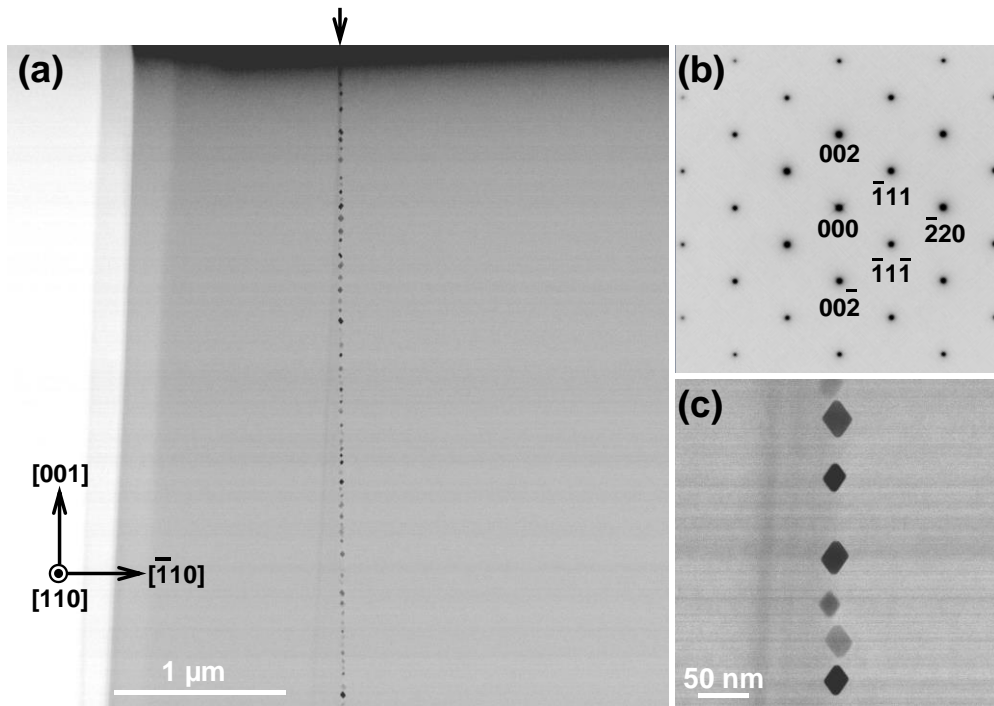


FIGURE 3

Microstructure of flash-healed microcrack near the positive electrode: (a) HAADF-STEM image, (b) SAD patterns that include both crystal sides along a row of pores, and a (c) magnified HAADF-STEM image of the pores.

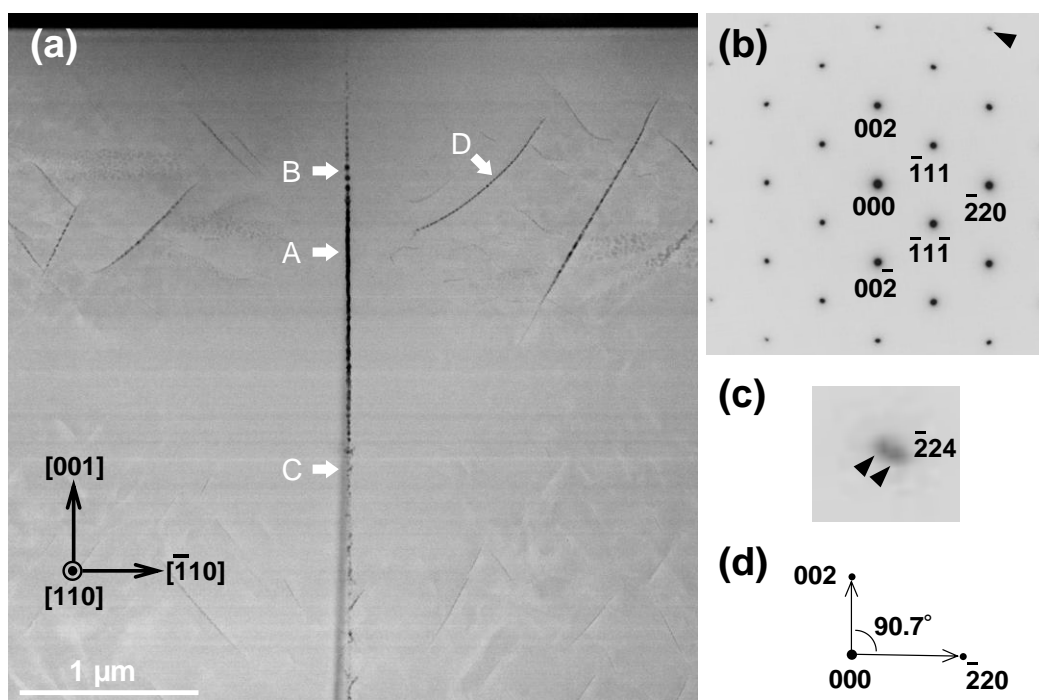


FIGURE 4

Microstructure of a flash-healed microcrack near the negative electrode: (a) HAADF-STEM image, (b) SAD patterns that include both crystal sides along a row of pores, (c) magnified diffraction spot of $\bar{2}24$, and a (d) schematic illustration showing the angle between the 002 and $\bar{2}20$ diffraction spots.

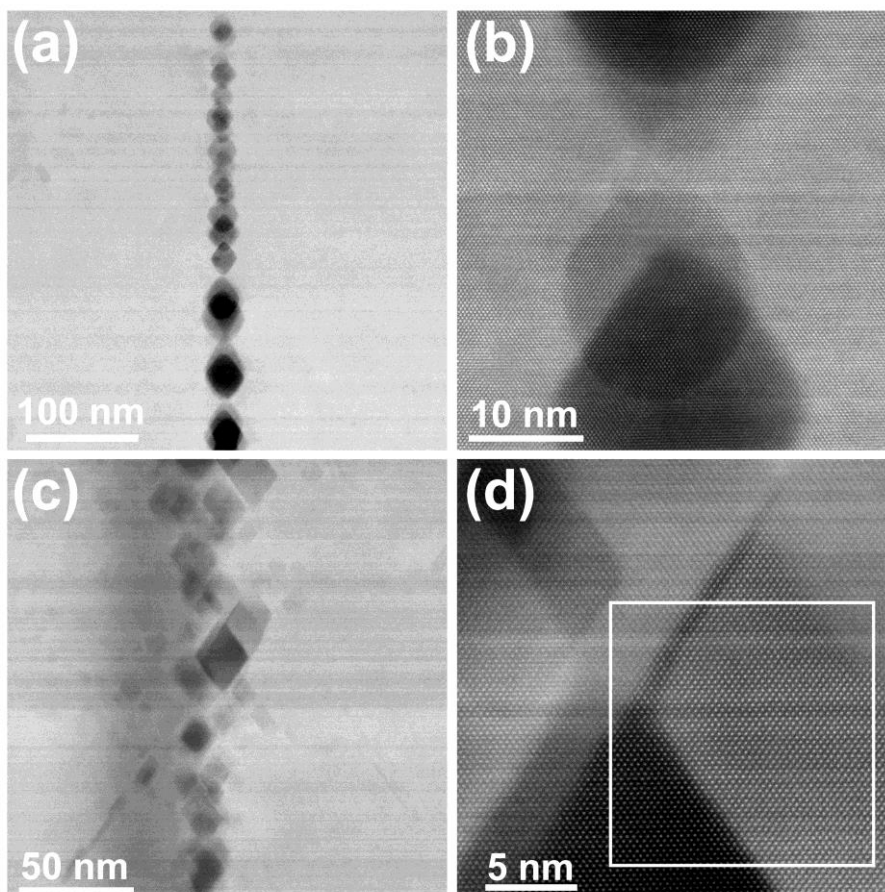


FIGURE 5

HAADF-STEM images taken from the areas indicated in Fig. 4(a): (a) and (b) from arrow B, and (c) and (d) from arrow C. A white box in (d) shows a scan area for EDS measurement that will be presented in energy dispersive spectrometry profile 2 of Fig. 6(c).

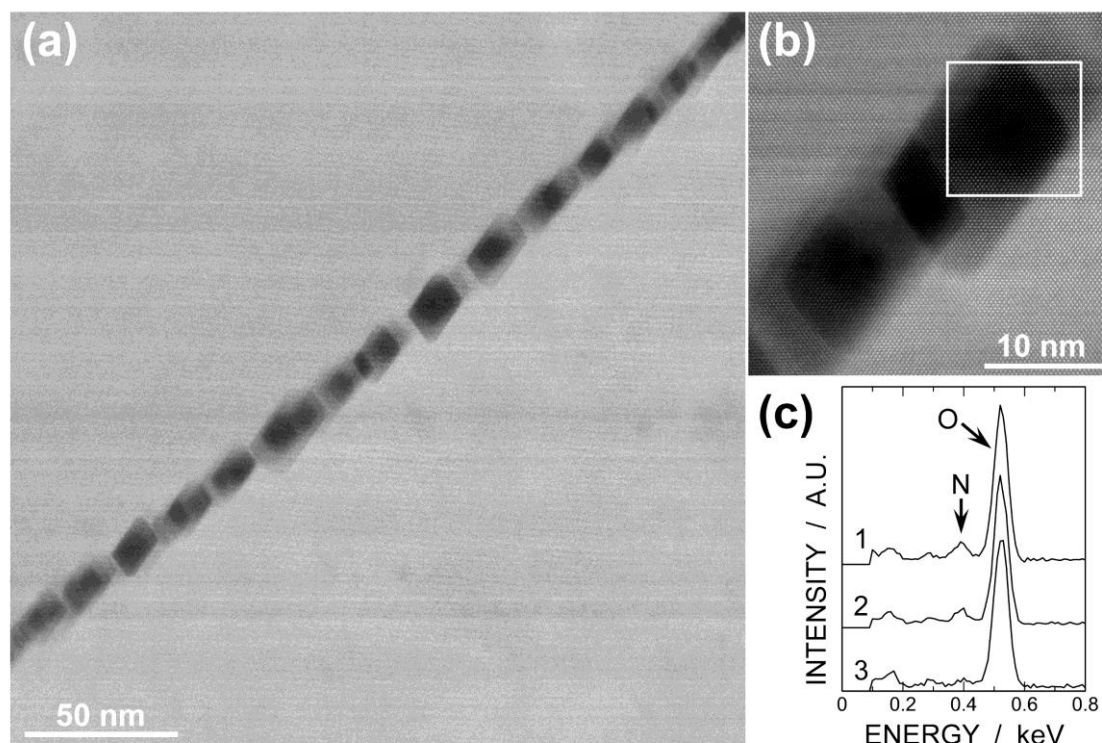


FIGURE 6

(a) and (b): HAADF-STEM images taken from the structure with a curved liner contrast indicated by arrow D in Fig. 4(a).

(c) Energy dispersive spectrometry profiles of 1) the white box area shown in Fig. 6(b), 2) the white box area shown in Fig. 5(d), and 3) the area about 50 nm away from the white box shown in (b) (crystal inside).

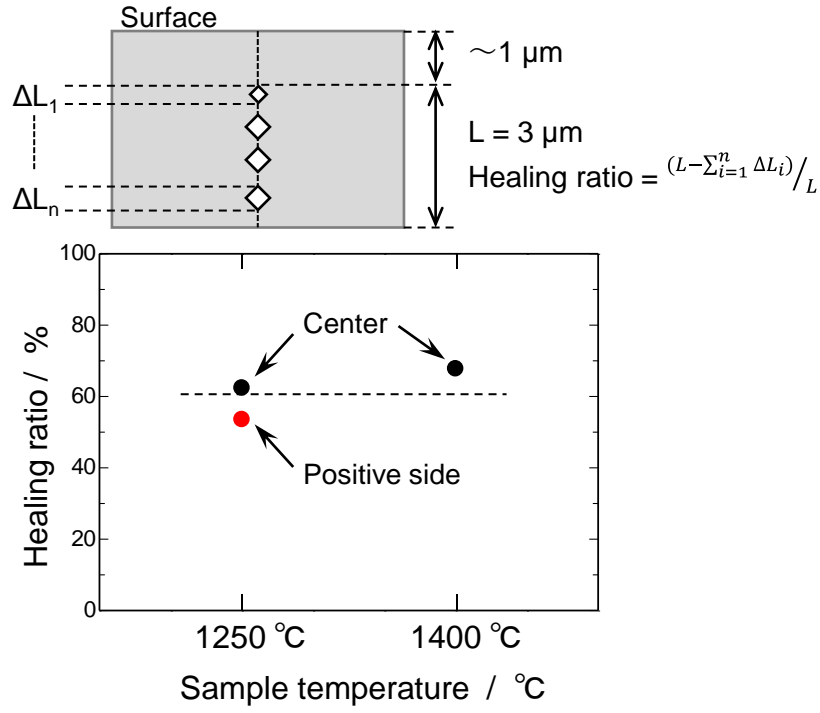


FIGURE 7

Schematic illustration showing how to estimate the healing ratio, and a plot showing healing ratios of flash-healed microcracks near the positive electrode (red dot) and indents at a center between the positive/negative electrodes (black dots)¹⁷⁾. Sample temperatures were calculated based on the volumetric power dissipations during flash healing.

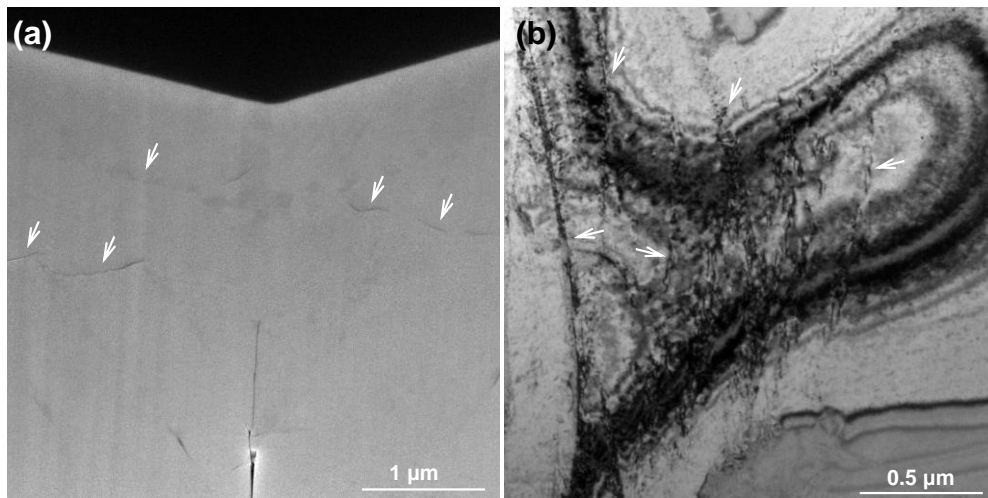


FIGURE 8

SEM image showing (a) a cross-section of the area below the indent of a pristine Vickers indent sample, and (b) a bright-field TEM image showing dislocations formed in the area below the Vickers indent.

Supplementary information

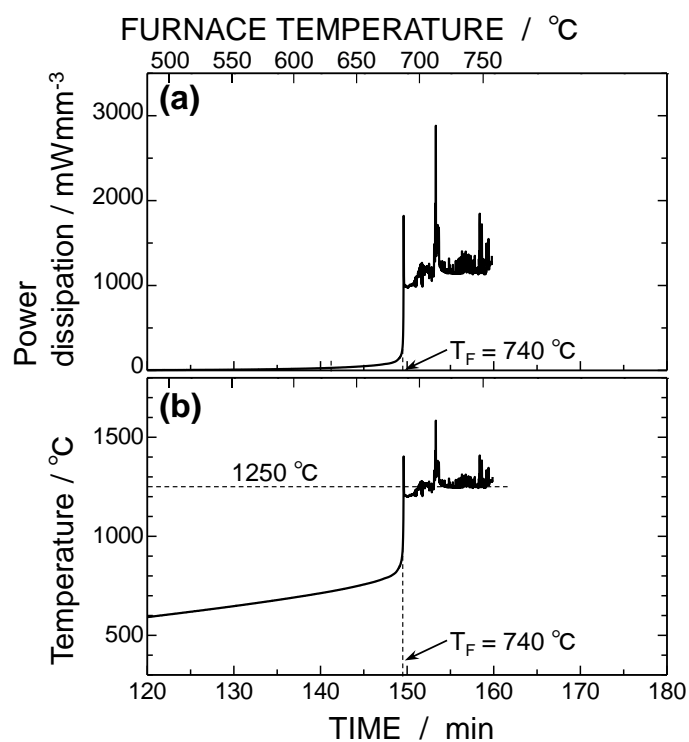


FIGURE S1

Plots showing the (a) power dissipation and (b) sample temperature versus processing time during flash healing¹⁷⁾.

Supplementary information

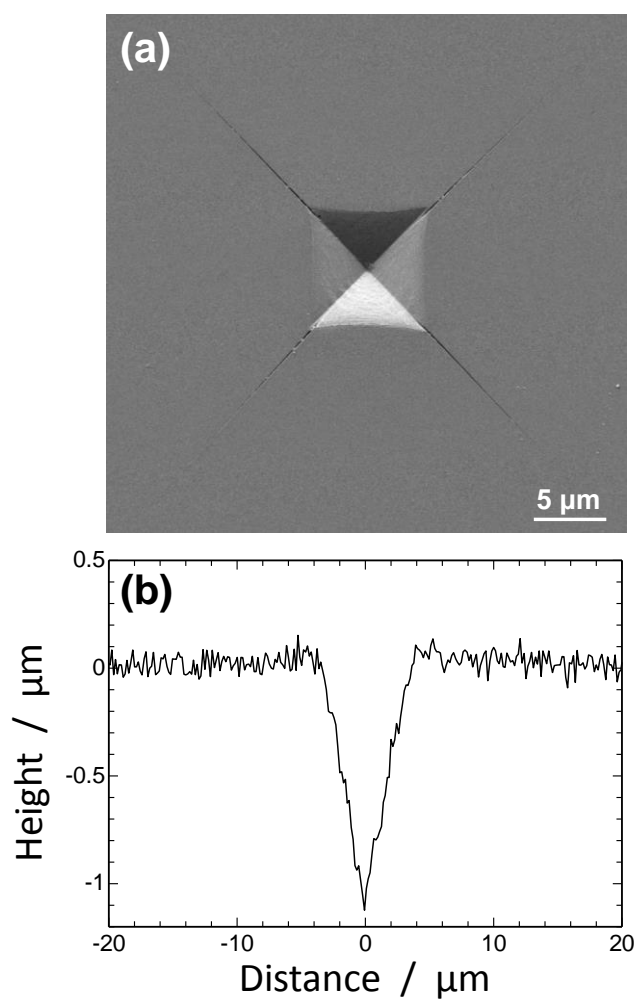


FIGURE S2

(a) SEM image and (b) height profile taken from a pristine Vickers indent²¹.